Article

Reverse Micelle Strategy for the Synthesis of MnOx–TiO2 Active Catalysts for NH3-Selective Catalytic Reduction of NOx at Both Low Temperature and Low Mn Content

Barbara Bonelli, Olimpia Tammaro, Ferenc Martinovic, Roberto Nasi, Gianfranco Dell'Agli, Paola Rivolo, Fabrizio Giorgis, Nicoletta Ditaranto, Fabio Alessandro Deorsola, and Serena Esposito*

Read Online

ACCESS | Metrics & More | Article Recommendations | SI Supporting Information

ABSTRACT: MnOx–TiO2 catalysts (0, 1, 5, and 10 wt % Mn nominal content) for NH3-SCR (selective catalytic reduction) of NOx have been synthesized by the reverse micelle-assisted sol–gel procedure, with the aim of improving the dispersion of the active phase, usually poor when obtained by other synthesis methods (e.g., impregnation) and thereby lowering its amount. For comparison, a sample at nominal 10 wt % Mn was obtained by impregnation of the (undoped) TiO2 sample. The catalysts were characterized by using an integrated multitechnique approach, encompassing X-ray diffraction followed by Rietveld refinement, micro-Raman spectroscopy, N2 isotherm measurement at −196 °C, energy-dispersive X-ray analysis, diffuse reflectance UV–vis spectroscopy, temperature-programmed reduction technique, and X-ray photoelectron spectroscopy. The obtained results prove that the reverse micelle sol–gel approach allowed for enhancing the catalytic activity, in that the catalysts were active in a broad temperature range at a substantially low Mn loading, as compared to the impregnated catalyst. Particularly, the 5 wt % Mn catalyst showed the best NH3-SCR activity in terms of both NOx conversion (ca. 90%) and the amount of produced N2O (ca. 50 ppm) in the 200–250 °C temperature range.
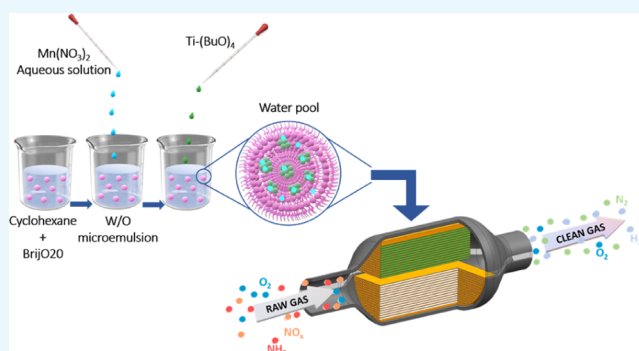
1. INTRODUCTION

Nitrogen oxides (NOx) are still the major air pollutants that are discharged by both combustion engines, as the primary mobile source, and by power plants and nitric acid production plants, as stationary ones.[1,2] To reduce NOx emissions, multiple denitrification (deNOx) technologies have emerged; among them, the selective catalytic reduction (SCR) with ammonia (NH3-SCR) is one of the most reliable and common methods due to NOx reduction efficiency, durable performance, and reasonable costs.[3−5]

TiO2-supported V2O5 catalysts, promoted by either WO3 or MoO3, have been recognized as the most important commercial system in NH3-SCR, in the name of their high activity and resistance to SO2 poisoning.[4,6−8] However, the disadvantages of the narrow range of operating temperature (300−400 °C) and of the fast and irreversible deactivation above 450 °C lead to a pressing need for SCR catalysts characterized by both low cost and low T efficiency.[6−9]

Various transition metal oxides have also been reported to efficiently catalyze SCR reactions at low T, where the doping metal content reaches up to 30 wt %.[10] Manganese oxides (MnOx) have shown excellent performance, mostly ascribed to various types of labile oxygen species and Mn oxidation states (Mn2+, Mn3+, and Mn4+), which can have a significant role in

accomplishing the catalytic cycle enhancing the NO oxidation, the nitrate formation, and the NH3 activation steps.[11−15] Furthermore, Mn is less toxic than other transition metals like V, Co, and Ni and is highly abundant in soil.

The NH3-SCR cycle typically involves the adsorption and activation of both NO and NH3 molecules on the catalyst active sites.[10,16] Optimizing the interaction between the two activated molecules is crucial to avoid undesired parallel reactions, most notably NH3 overoxidation and N2O production.[17,18]

The need of satisfactory catalytic activity can be fulfilled by tailoring the textural features of the support and the redox properties of the active species. The main principle is that the catalyst should be dispersed on a suitable support to obtain stable active species. In addition, it is important that there is adequate metal-support interaction and optimum performance
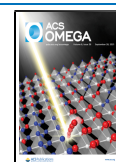
at low metal loading, which consequently reduces the cost of the catalyst. Impregnation and coprecipitation methods are applied to produce a wide range of materials but usually provide a poor control on the formed species and their dispersion and on their interaction with the support. Among the different oxides used as a support for the SCR catalyst, TiO_2 offers excellent dispersion of the active components, proving to be an ideal candidate support for Mn-based low-temperature SCR catalysts.[15]

Ettireddy et al. explored the effect of Mn loading by wet impregnation of different TiO_2 phases: anatase was identified as the best support with an optimal Mn content of about 17 wt %, corresponding to monolayer coverage.[19] On the other hand, plentiful papers in the literature report that significant NO_x conversion and N_2 selectivity are obtained by using catalysts having Mn loading larger than 15 wt %.[20,21]

Bimetallic systems are often used to improve the catalytic performance. Putluru et al. prepared a series of Mn/TiO_2 and Fe-promoted Mn/TiO_2 catalysts by both precipitation and impregnation methods, and the results were discussed by directly comparing their activity with that of commercial $V_2O_5-WO_3/TiO_2$ (3 wt % V_2O_5, 7 wt % WO_3).[22] The catalysts prepared by precipitation exhibited superior low temperature activity with respect to the impregnated ones, reaching 96% NO conversion with an Fe-promoted Mn/TiO_2 catalyst. Nevertheless, the required total active metal content was 25 wt %, whereas NO conversion values dropped to 65% for a metal content below 10 wt %.

In this scenario, the sol−gel method is an outstanding route providing a potential control of the doping process. Sol−gel is a wet chemical process where a liquid "sol" transforms into a "gel" phase by competition, at the molecular level, between the reactions responsible for the formation and the growth of colloidal particles.

Its versatility and mild conditions allow for tailoring the textural and surface properties through the synthesis parameters, making the sol−gel processing a powerful tool for the synthesis of materials.[23−30]

A superior dispersion with no detectable sintering or formation of MnO_x crystalline phases up to a Mn/Ti molar ratio equal to 0.4 was obtained by traditional sol−gel preparation. Nevertheless, the initial expectations of an improved catalytic activity at Mn loading below 20 wt % were not met.[31] The same authors also explored the effect of transition metals in addition to Mn/TiO_2-based catalysts for low temperature SCR. Activity was enhanced by adding Fe [Fe(0.1)−Mn(0.4)/TiO_2] via the one pot sol−gel procedure, and the NO conversion was more than 90% at about 100 °C.[13]

The work by Kim et al.[32] aimed at investigating the effect of the preparation method on the $deNO_x$ activity of the Mn/TiO_2-based catalyst. The sol−gel approach allowed for reaching a better $deNO_x$ performance as compared to an impregnated Mn/TiO_2 catalyst in the 150−350 °C temperature range. At 250 °C, 90% NO conversion was achieved with the sol−gel catalyst at the highest Mn content (30 wt %). The observed enhancement of the $deNO_x$ activity due to the increase in the Mn content was ascribed to the remarkable dispersion of MnO_2 on the catalyst surface by the efficient incorporation of Mn into the TiO_2 matrix during the sol−gel preparation.[32]

Although sol−gel catalysts are more efficient with respect to those obtained by conventional methods (e.g., impregnation), several shortcomings of the reported systems still need to be addressed, including the narrow temperature range, the substantial Mn content, and to some extent, the low N_2 selectivity.

Among the different types of chemical processes that may be considered under the heading of "sol−gel", the reverse micelle approach provides a favorable microenvironment to control the nucleation and growth of nanoparticles (NPs), simultaneously enhancing the metal dispersion. Reverse micelles are nanometric droplets of the aqueous phase stabilized by surfactants in an organic phase, and the rate of hydrolysis and condensation are driven by the frequency of intermicellar exchanges and by the water content in the micelle core, in addition to the structure-directing role of the surfactant. The supramolecular template sol−gel technique overcomes the obstacles encountered in more traditional procedures, where the high hydrolysis rate makes the handling of transition metal alkoxides not straightforward. In addition, transition metals often exhibit several (stable) coordination states, and when coordinatively unsaturated, they are able to expand their coordination sphere by solvation or alkoxy bridging.[33] The vigorous reaction of Ti alkoxides with water leads to (undesired) formation of Ti oxo/hydroxo precipitates. The most common inhibitors are complexing ligands, β-diketones, polyhydroxy acids, or carboxylic acids, which reduce the reactivity of Ti alkoxides by increasing its coordination number and decreasing the number of easily hydrolyzable groups.[33]

In this work, a one-pot reverse micelle strategy has been adopted to prepare TiO_2-supported MnO_x species at low metal content (namely, 1, 5, and 10 wt % Mn). A thorough physicochemical characterization was carried out by X-ray diffraction (XRD) followed by Rietveld refinement, microRaman spectroscopy, N_2 isotherm measurement at −196 °C, energy-dispersive X-ray (EDX) analysis, DR (diffuse reflectance) UV−vis spectroscopy, temperature-programmed reduction (TPR) technique, and X-ray photoelectron spectroscopy (XPS) to gain insights into both structural and surface properties of the MnO_x-TiO_2 catalysts. The activity in the SCR of NO_x with NH_3 was evaluated by directly comparing the sol−gel MnO_x-TiO_2 catalysts with a catalyst prepared by impregnating with the same Mn precursor the (undoped) TiO_2 prepared by the same reverse micelle sol−gel method. The results were discussed in relation with the structural and surface features, in order to explain the enhanced performance of the sol−gel-derived catalysts, in terms of both low T activity and low Mn content, obtained during the NH_3 SCR catalytic tests.

2. RESULTS AND DISCUSSION

2.1. Structural and Textural Properties of the Catalysts.
The diffraction patterns of the various catalysts, displayed in Figure 1, reveal the occurring phases. At a first glance, all the studied samples are multiphase, with anatase (A) as the main phase along with the presence of minor phases, which are labeled B (for brookite), R (for rutile), and P (for pyrolusite, i.e., β-MnO_2); furthermore, the pronounced broadness of the XRD peaks suggests a low degree of crystallinity, that is, a nanometric crystal size of the various phases.
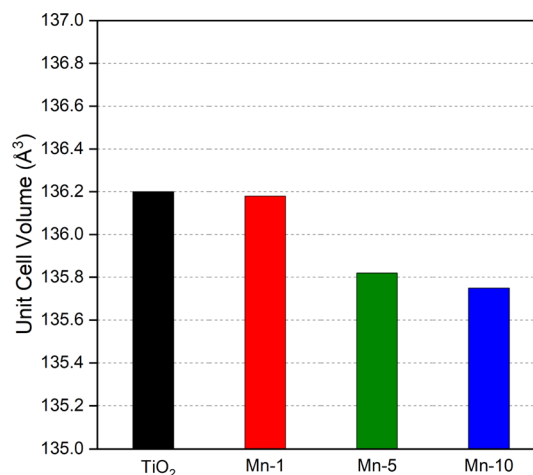
The amount of each phase, the anatase cell parameters, and the crystal size were determined by Rietveld refinement (data shown in Table 1). Due to their low content, for the minor phases, the only refined parameter was their amount, whereas the other parameters were kept constant or equal to anatase,
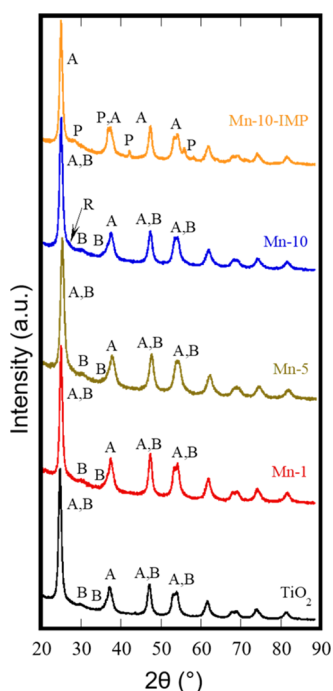
Figure 1. XRPD patterns of the prepared samples; the different crystalline phases are labeled as follows: (A) anatase, (B) brookite, (R) rutile, and (P) Pyrolusite.

Figure 2. Anatase unit cell volume of the sol−gel prepared samples.

when possible. The plots of the refinements (data not shown) confirm the very good quality of all the refinements as confirmed by the values of sigma and R_{wp} (weighted profile R-factor) reported in Table 1.

According to the data given in Table 1, the phase composition of the sol−gel samples is almost the same up to 5 wt % Mn, whereas with the Mn-10 catalyst, the appearance of rutile induces a non-negligible reduction of the anatase content. This finding is not surprising, considering that the Mn dopant addition is reported to promote the anatase to rutile (ATR) phase transformation.[34] With all these catalysts, no trace of Mn-containing crystalline phases was detected. The anatase lattice parameter suggests that at least a certain amount of Mn^{4+} ions has been dissolved in the anatase matrix by substituting Ti^{4+} cations. Figure 2 shows that TiO_2 and Mn-1 have a very similar unit cell, in agreement with the low Mn content of the latter sample, and then, a progressive shrinking of the unit cell occurs, perfectly compatible with a partial substitution of Ti^{4+} ions (octahedral Ti^{4+} has r = 0.605 Å[35]) by Mn^{4+} ions (octahedral Mn^{4+} has r = 0.53 Å[35]). Therefore, by

increasing the amount of Mn in the sol−gel process, the metal tends to dissolve within the anatase phase. The impregnated sample has a completely different behavior; indeed, TiO_2 is present only as an anatase phase, likely due to the calcination step following the impregnation, whereas Mn occurs in the pyrolusite (β-MnO_2) phase. The amount of pyrolusite calculated by Rietveld refinement (almost 9 wt %) is very close to the nominal one (10 wt %), indicating that only a small (if any) fraction of Mn was dissolved in the TiO_2 matrix, in agreement with the adopted (impregnation) procedure.

As a further confirmation, the anatase cell volume of Mn-10-IMP is similar to that of the TiO_2 support, likely indicating that in the impregnated sample, the two oxides crystallized independently and no solid solution of MnO_2 in TiO_2 formed. Therefore, the insertion on Mn inside the anatase lattice is possible only if the system is mixed at an atomic level (here, during the reverse micelle-assisted sol−gel synthesis) and not when mixing occurs at a large scale, as during impregnation.

The reported XRD results strongly evidence the effectiveness of the reverse micelle sol−gel approach where the nanometer-size aqueous systems promote the intimated contact between the precursors. The surfactant, indeed, provides a cagelike environment that favors an excellent control of the final powder stoichiometry with the possibility of obtaining homogeneity and mixing at the atomic scale, ultimately favoring the inclusion of Mn in the studied samples.

The Raman spectra of the prepared catalysts are shown in Figure 3a,b 100−275 and 275−1200 cm^{-1} range: the typical anatase TiO_2 Raman scattering peaks (black line, Figure 3a,b)

Table 1. Determination of Anatase Cell Parameters, Different Phase Contents, and Crystal Size as Obtained by Rietveld Refinement

	TiO₂	Mn-1	Mn-5	Mn-10	Mn-10-IMP
a (Å) anatase	3.78898	3.789194	3.787906	3.78774	3.787105
b (Å) anatase	9.48788	9.483329	9.468461	9.463282	9.484697
cell volume (Å³)	136.21	136.16	135.86	135.77	136.03
anatase (wt %)	91	90.49	91.23	86.19	91.42
brookite (wt %)	9	9.51	8.77	10.7	
rutile (wt %)				3.11	
pyrolusite (wt %)					8.57
crystal size anatase (Å³)	163	179	153	162	190
sigma	1.98	1.63	1.71	1.57	1.89
R_{wp}	4.27	4.34	4.23	3.65	4.17
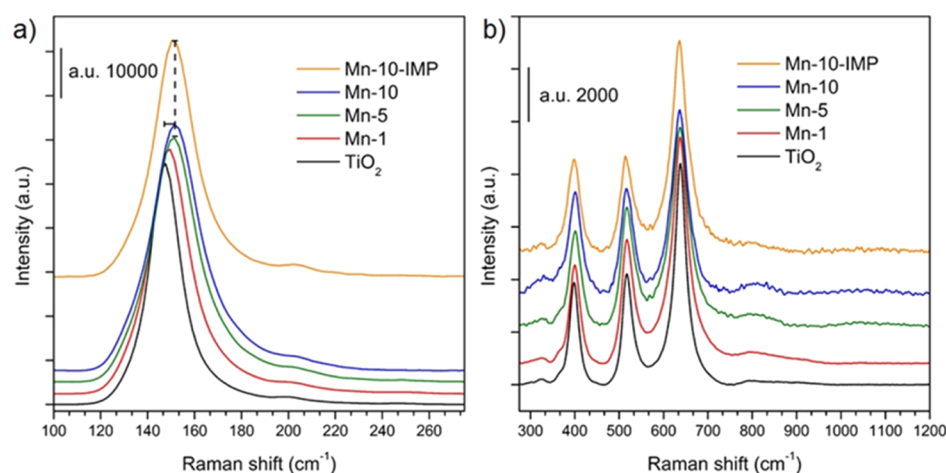
Figure 3. Raman spectra of the following samples: TiO_2 (black curve); Mn-1 (red curve), Mn-5 (green curve), Mn-10 (blue curve), and Mn-10-IMP (orange curve). The spectra are reported in two (complementary) sections, (a) (100−275) and (b) (275−1200 cm^{-1}) in order to allow the reader to appreciate scattering bands with very different intensities.

are seen at 144 (E_g), 198 (E_g), 320 (one of the weak two-phonon bands), 397 (B_{1g}), 516 ($A_{1g} + B_{1g}$), 639 (E_g), and 795 (B_{1g}) cm^{-1}.[36] Some weak signals, due to the low content of brookite TiO_2 and superimposed to the anatase spectrum, are discernible at 247 (A_{1g}), 322 (B_{1g}), 366 (B_{2g}) cm^{-1}, as well. In addition, the known[36] strongest modes of brookite at 128 (A_{1g}) and 636 (A_{1g}) cm^{-1} are completely hidden by the nearly coincident modes of anatase.

For all the TiO_2 phases, the modes below 400 cm^{-1} are ascribable to O−Ti−O bending vibrations and the ones above 400 cm^{-1} are due to Ti−O stretching vibrations. Thus, both types of modes could be affected by the possible incorporation of Mn. In particular, the most sensitive one is the E_g peak at 144 cm^{-1}, as it is much responsive to local oxygen coordination surrounding the metal ion. Actually, as shown in Figure 3a, the blue shift (i.e., toward higher wavenumbers) of the 144 cm^{-1} peak, which also becomes asymmetric and larger, increases with the Mn content for the sol−gel catalysts, owing to the disruption of the topological order in the TiO_2 matrix, related to the probable insertion of Mn ions. Moreover, such Mn species could generate point defects in the TiO_2 lattice and its contraction, in agreement with the evolution of such bands.[37] Moreover, by comparing the Mn-10 spectrum (blue line) with Mn-10-IMP (orange line), a shift of the 144 cm^{-1} peak occurs (Figure 3a), similar to the one observed for the Mn-5 sample, but the peak does not lose its symmetry. For this reason, the broad anatase peak centered at 198 cm^{-1} becomes more intense and, finally, Mn incorporation cannot be inferred by Raman spectroscopy.

Because the modes of the vibrations due to MnO_2 and Mn_2O_3 species are overlapped to those of TiO_2 in the same spectral region, a subtraction (Figure S1) of the undoped TiO_2 spectrum to each of the Mn-doped TiO_2 spectra has been performed, in order to single out any Mn-related bands. In Figure 3b, the 530 and 651 cm^{-1} peaks (related to amorphous MnO_2 and Mn_2O_3, respectively) are visible with the Mn-1, Mn-5, and Mn-10 samples.[37] Their intensities increase with the Mn nominal content. With Mn-10, the 318 and 382 cm^{-1} modes, assigned to Mn_2O_3, are observable,[38] and for Mn-5 and Mn-10, a broad band centered at 1050 cm^{-1} related to amorphous MnO_2 appears. The Mn-10-IMP spectrum is quite superimposable to the undoped TiO_2 spectrum (no peak shift

nor width enlargement are observable), and it does not show MnO_x-related modes, except for the very broad signal at 1050 cm^{-1}. Moreover, no trace of pyrolusite, instead detected by XRD, could be singled out (the reference RRUFF Project Raman pyrolusite spectrum being not reported), thus suggesting that the formed Mn oxides (detected by both XRD and DR-UV−vis spectroscopy, *vide infra*) are not homogenously dispersed on the surface of TiO_2 and/or that their amount is below the sensitivity of the Raman technique in the examined spots. This result confirms that impregnation does not allow a fine dispersion of Mn on the sample, whereas the sol−gel method does. Indeed, the EDX analysis (Table 2)

Table 2. Textural Properties of the Studied Samples as Determined by N_2 Isotherms at −196 °C, FESEM and EDX Analyses

| sample	BET SSA (m^2 g^{-1})	total pore volume (cm^3 g^{-1})	micropore volume^a (cm^3 g^{-1})	EDX (nominal) Mn/Ti atomic ratio
TiO_2	70	0.090	0.0002	
Mn-1	57	0.096	0.0017	0.0164(0.0147)
Mn-5	76	0.109	0.0017	0.0656(0.0765)
Mn-10	68	0.102	0.0004	0.106(0.161)
Mn-10-IMP	40	0.070		0.604 (0.161)

^{a}As obtained according to the *t*-plot method.

shows Mn/Ti atomic ratios close to nominal values for the sol−gel catalysts, whereas the value determined with the impregnated sample is very high, likely due to the aforementioned heterogeneity induced by the impregnation technique.

Table 2 also reports the textural properties of the catalysts as obtained by N_2 physisorption at −196 °C. The samples showed type IV isotherms (Figure S2) with a H2 hysteresis loop, characteristic of mesoporous solids with interparticle porosity. As expected, the impregnated sample shows a drop in both the surface area and pore volume, whereas the other samples show Brunauer−Emmett−Teller (BET) specific surface area (SSA) values in the 57−76 m^2 g^{-1} range and total pore volume values in the 0.09−0.102 cm^3 g^{-1} range, indicating a limited effect of Mn doping on the sample porosity.

The field-emission scanning electron microscopy (FESEM) analysis (Figure S3) showed the occurrence of spherical NPs with uniform shape and size, forming large agglomerates/aggregates, likely due to NP coalescence after calcination. The Mn-10-IMP sample showed instead larger NPs but still with a quasispherical shape and forming large agglomerates/aggregates.

2.2. Characterization of Bulk and Surface Mn Species.

The DR UV−vis spectra of the studied catalysts are reported in Figure 4. As expected, TiO_2 shows a typical UV−vis spectrum
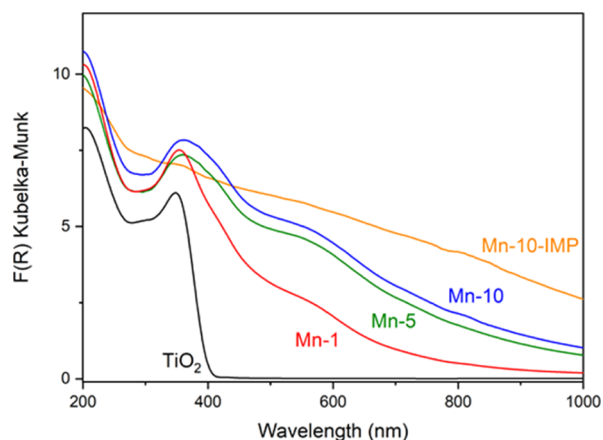
Figure 4. DR UV−vis spectra of the following samples: TiO_2 (black curve); Mn-1 (red curve), Mn-5 (green curve), Mn-10 (blue curve), and Mn-10-IMP (orange curve).

due to the CT (charge-transfer) transitions from O^{2-} to Ti^{4+}: a band gap (E_g) of 3.01 eV has been calculated by applying the Tauc's plot method and assuming an indirect semiconductor behavior $(F(R)*(h\upsilon))^{1/2}$ in agreement with the fact that it mainly contains anatase (indirect semiconductor), with a minor amount of brookite (direct semiconductor). The DR UV−vis spectrum of Mn-10-IMP, instead, shows a broad absorption in the whole investigated range and resembles the literature spectra usually reported for MnO_2.[39] This result is in agreement with XRD patterns (*vide supra*), showing the occurrence of pyrolusite in the sample.

Considering the Mn-doped catalysts obtained by sol−gel, the Mn-1 spectrum shows two broad and intense absorptions at about 420 and 560 nm, that is, in the region of Mn ion d−d transitions (360−800 nm). At higher Mn contents (i.e., Mn-5 and Mn-10 spectra), the two bands become more intense, another component is observed at ca. 390 nm, and simultaneously, the O^{2-} to Ti^{4+} CT band (at 350 nm in TiO_2) suffers a slight red shift (i.e., toward longer wavelength), likely due to Mn doping by inclusion in the TiO_2 lattice, as shown by XRD. The component at 390 nm is assigned in the literature to d−d transitions of octahedral Mn^{4+} ions,[40]

whereas the other two bands are ascribed to different MnO_x species, likely amorphous (as confirmed by both XRD and Raman techniques) and located at the NP surface, in agreement with XPS results (*vide infra*).[41]

The catalysts prepared by sol−gel synthesis show a progressive decrease of the E_g value to 2.06 (Mn-1), 1.64 (Mn-5), and 2.00 eV, (Mn-10) confirming that, along with the formation of surface MnO_x species, bulk Mn doping occurs by using the adopted synthesis technique, in agreement with XRD results (*vide supra*). Moreover, this result is in agreement with both experimental[42] and theoretical studies,[43] the latter showing that substitution of Ti^{4+} ions by Mn ions leads to a remarkable red shift of the optical absorption edge both by overall reduction of the band gap and introduction of curvy intermediate bands into the forbidden gap. The (unexpected) increase of the band gap energy with the Mn-10 sample may be due to an extensive doping, which can lead to the well-known Moss-Burnstein effect occurring at a high dopant content. Indeed, with Mo-doped TiO_2 samples with the similar metal content obtained by the same synthesis procedure,[44] the same effect was observed; this result is another proof of the effectiveness of the sol−gel synthesis in the doping of TiO_2 by heteroatom ions (here, Mn).

The surface chemical composition of the Mn-doped TiO_2 catalysts has been investigated by means of XPS, allowing for both a qualitative and quantitative analysis of the surface chemical composition. Table 3 reports the surface elemental composition (at. %) along with the Mn/Ti atomic ratios, as derived by the quantification of the O 1s, Mn 2p, and Ti 2p spectral regions.

The surface amount of Mn was found to increase with the nominal Mn content, as shown by both the absolute Mn at. % and the Mn/Ti atomic ratio values reported in Table 3, in agreement with a previous work concerning Mo-doped TiO_2 samples obtained by means of the same synthetic procedure.[44,45] Also, the impregnation procedure resulted in a higher surface Mn availability, as compared to the sol−gel process, as seen by comparing the Mn/Ti ratio of the Mn-10-IMP and the Mn-10 samples.

In order to gather information on the surface chemical speciation and Mn oxidation states, a curve-fitting procedure was applied to the Ti 2p, Mn 2p, and O 1s high-resolution XP spectra. The Ti 2p spectral region showed the typical spin−orbit splitting doublet of Ti $2p_{3/2}$ and Ti $2p_{1/2}$ species with binding energy (BE) and separation values consistent with Ti^{4+} in the TiO_2 lattice (Figure S4). The Mn 2p and O 1s XP regions (Figures 5 and 6, respectively) provided interesting results on the possible oxidation states of Mn and oxygen surface vacancies.

Mn 2p XP spectra can be very complex due to the coupling of angular momenta associated with partially filled core and valence shells containing unpaired electrons. This can create a

Table 3. XPS Surface Elemental Composition of Mn-Doped TiO_2 Catalysts. The Values are Averaged out of at Least Three Replicates and are Reported as Mean Value $\pm$ 1S
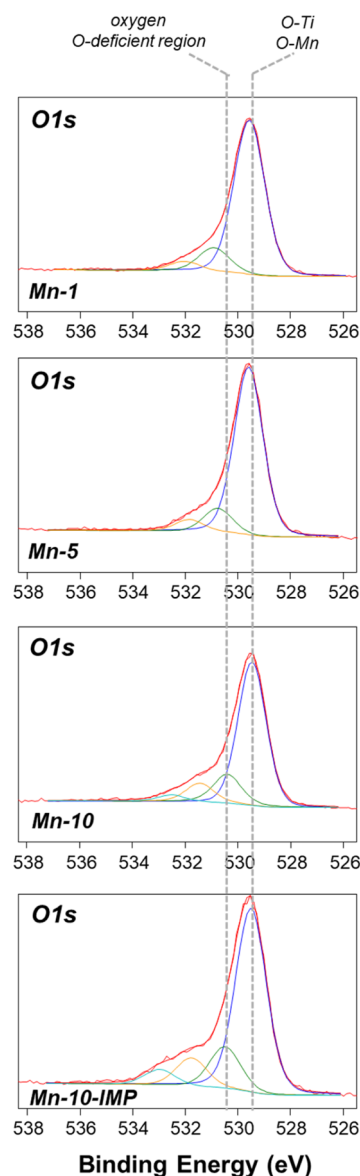
Sample	XPS surface elemental composition (at. %)			
	Mn	Ti	O	Mn/Ti atomic ratio
Mn-1	1.1 ± 0.2	26.5 ± 1.6	72.4 ± 1.6	0.042 ± 0.004
Mn-5	2.6 ± 0.3	26.3 ± 1.1	71.1 ± 1.4	0.10 ± 0.01
Mn-10	3.5 ± 0.5	24 ± 2	73 ± 2	0.15 ± 0.02
Mn-10-IMP	10.5 ± 0.5	17.5 ± 1.0	72.3 ± 1.3	0.58 ± 0.04
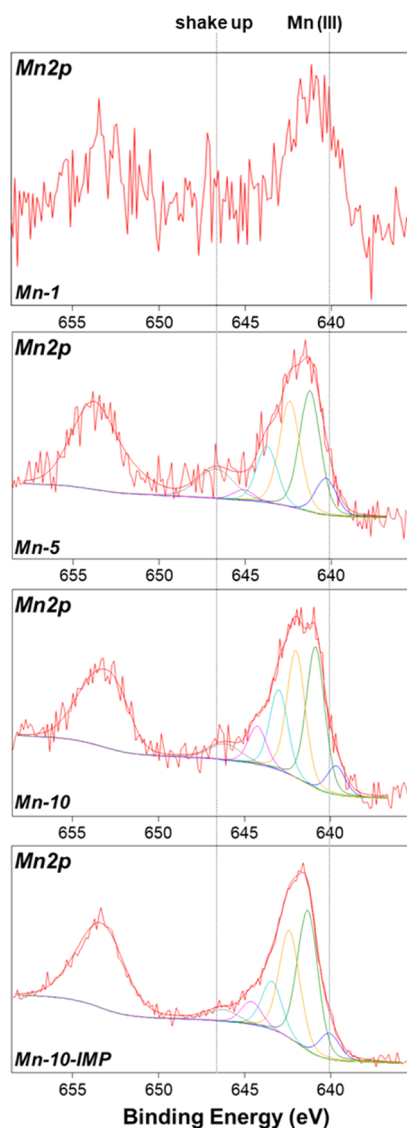
Figure 5. Mn 2p XP spectra for all Mn-doped catalysts. Curve fitting has been applied only to the $2p_{3/2}$ peak component.

Figure 6. O 1s XP spectra and corresponding curve fittings as obtained with the samples (from top to bottom): Mn-1, Mn-5, Mn-10, and Mn-10-IMP.

number of final states, which will manifest in the XP spectrum in the form of multiplet splitting. In particular, out of the six stable manganese oxidation states (0, +2, +3, +4, +5, and +7), three have significant multiplet splitting (Mn^{2+}, Mn^{3+}, and Mn^{4+}), and thus, the qualitative and quantitative XPS investigation of Mn-containing samples is particularly challenging.[11,46−49] The separation of the $2p_{3/2}$ and $2p_{1/2}$ spin−orbit splitting components of Mn is large enough to consider only the (more intense) $2p_{3/2}$ signal and its associated structure.

The curve fitting procedure applied to the Mn $2p_{3/2}$ XP spectra of Mn-1 to Mn-10-IMP samples is reported in Figure 5. Due to the complexity of this signal, a first parameter to focus on could be the main peak shape because it presents some detailed features depending on the presence/prevalence of the specific oxidation state, as described by Biesinger et al. who reported Mn 2p spectra for various standard samples and discussed in detail the corresponding fitting parameters.[46] Comparing the Mn 2p spectra of the present work with those by Biesinger et al., it is possible to observe the occurrence of a shake-up satellite around 646.0 ± 0.2 eV, suggestive of surface Mn(II) species, whose relative abundance decreases as the

total Mn % increases (see Table S1 in the Supporting Information file). It is close to 9% in the Mn-5 sample and goes down to 3% in the Mn-10-IMP sample. Also, a prominent shoulder at lower BE values (640.0 ± 0.2 eV), typical of Mn(III), could be identified in all the samples with a comparable relative abundance. With the Mn-10-IMP sample, it is also possible to identify a peak shape and a multiplet splitting strongly resembling those of Mn(III) species. The Mn $2p_{3/2}$ XP spectrum of Mn-1 was not curve fitted, due to the very low signal-to-noise ratio, but the general peak shape is close to those of both Mn-5 and Mn-10. A further spectral feature is the 2p spin−orbit splitting value; it is shown to increase as the Mn oxidation state increases.[17] The value for all our catalysts is always 11.6 ± 0.1 eV, compatible with the presence of both Mn(II) and Mn(III). All those findings indicated that a mix of Mn(II) and Mn(III) is generally distinguishable at the surface of the Mn-doped catalysts: Mn(II) species could be hypothesized to be more abundant in the case of the sol−gel samples and their relative amount

decreasing at a higher Mn content; conversely, Mn(III) species are predominant at the surface of the impregnated catalyst. Moreover, due to complexity of Mn 2p multiplet splitting, the occurrence of small amounts of Mn(IV) species could not be excluded, especially in the Mn-10-IMP sample on the base of the main peak shape. All these experimental evidences are confirmed by TPR analysis (*vide infra*).

The curve-fitted O 1s XP spectra are reported in Figure 6; the curve fittings shown from three (with the Mn-1 and Mn-5 samples) to four peak components (with the Mn-10 and Mn-10-IMP samples). The lowest BE peak is due to lattice oxygen species bonded to Ti and/or Mn (529.7 ± 0.2 eV), whereas the BE peak at around 531.4 ± 0.3 eV is attributed to nonlattice oxygen/OH species. Finally, the component at 530.5 ± 0.1 eV is due to oxygen in oxygen-deficient regions, whereas the highest BE peak (at 533.2 ± 0.2 eV) is ascribed to adsorbed/structural water.[50,51] It is important to notice how the amount of oxygen vacancies increases with the dopant concentration, as can be derived by the relative abundance of the peak component at 530.5 ± 0.1 eV, which is around 10−11% in Mn-5 and increases up to 16% in Mn-10 and Mn-10-IMP. As a whole, XPS analysis showed the occurrence of surface Mn species at the variable oxidation state [Mn(II) species being mainly found on the samples prepared by sol−gel]. Correspondingly, oxygen vacancies are observed due to the charge balance. Their occurrence in the Mn-10-IMP sample shows that the surface composition of pyrolusite differs from that of its bulk because only Mn^{2+} and Mn^{3+} species are observed by XPS.

Moreover, comparison of the Mn/Ti atomic ratio at the surface (XPS) and in the bulk (EDX) shows the occurrence of a surface enrichment in Mn, as previously observed with another set of Mo-doped TiO_2 samples with the similar heteroatom content that were obtained by the same synthesis procedure.[44]

The occurrence of different redox species and their dispersion at the catalyst surface is notoriously one of the main factors controlling the catalytic activity in the studied reaction. The redox ability of the catalysts was investigated by H_2-TPR, and the corresponding results are shown in Figure 7. The amount of H_2 consumption, reported in the following paragraphs, has been calculated in the range between room temperature and 500 °C.

According to the literature, the reduction process of manganese oxides covers a broad temperature range where (bulk) MnO_2 is successively reduced to lower oxidation states in the order $MnO_2 \rightarrow Mn_2O_3 \rightarrow Mn_3O_4 \rightarrow MnO$. The following T ranges are usually reported for the reduction of manganese oxides: 290−350 °C for MnO_2 reduction (but for pyrolusite, β-MnO_2, the T range increases up to 430 °C), 350−420 °C for Mn_2O_3 reduction to Mn_3O_4, and 450−500 °C for Mn_3O_4 reduction to MnO, which is not further reducible at the partial pressure of H_2 adopted during TPR analysis.[19,22,52,53] Reducibility is significantly affected by several other variables, like oxide dispersion and crystallite size, interaction with the support, synthesis method, and so forth.[19]

The undoped TiO_2 (not reported) showed some H_2 consumption, in agreement with the literature reporting that the support is not inert toward reduction.[54,55] In the TPR profile of the Mn-10-IMP catalyst (Figure 7), two sharp and well-defined reduction peaks were observed at ca. 325 and 435 °C, respectively. At higher T, no further peaks, ascribable to TiO_2 reduction, were identified. The TPR spectrum of Mn-10-
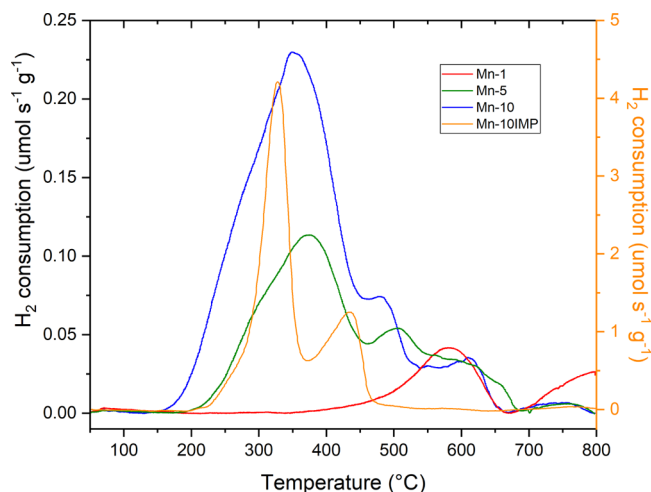
Figure 7. H_2-TPR profiles reported for the following samples: Mn-1 (red curve), Mn-5 (green curve), Mn-10 (blue curve), and Mn-10-IMP (orange curve). The left Y axis refers to the Mn-1, Mn-5, and Mn-10 samples; and the right Y axis refers to the Mn-10-IMP sample.

IMP likely corresponds to the reduction of MnO_2 to MnO, suggesting the following two-step reduction process: $MnO_2 \rightarrow Mn_2O_3/Mn_3O_4$ and $Mn_2O_3/Mn_3O_4 \rightarrow MnO$.[56] The related H_2 consumption was 91.8 μmol g^{-1}, which corresponded to a Mn average oxidation state of 3.9, in good agreement with XRD results, where crystalline β-MnO_2 was detected. The Mn-10 sample also showed two reduction peaks in the 250−550 °C range, indicating a two-step reduction process; however, the peaks were shifted to higher T as compared to the Mn-10-IMP sample, indicating an overall lower average Mn oxidation state.[57] This hypothesis is confirmed by the H_2 consumption that for the Mn-10 sample dropped to 16.3 μmol g^{-1}, from which an average Mn oxidation state of 2.5 was calculated. Moreover, the shape of the overall TPR profile is very broad and structured as compared to the Mn-10-IMP sample, indicating the likely occurrence of several nonstoichiometric MnO_x species, in agreement with Raman spectroscopy.[57]

Concerning the H_2 consumption above 500 °C, the peak at ca. 600 °C is due to the formation of Ti^{3+} species, forming oxygen deficient TiO_x species, whereas the minor H_2 consumption at c.a. 750 °C could be assigned to the reduction of the brookite phase, although in the same T range, other authors pointed out the occurrence of the ATR transition, which hampers a straightforward assignment in this case.[58−60]

The Mn-5 sample showed a H_2 consumption of 9.5 μmol g^{-1} corresponding to a calculated Mn average oxidation state of 2.3. The two reduction peaks observed for Mn-5 are even more shifted to higher T compared to Mn-10, in agreement with a slightly lower average oxidation state.

The TPR spectrum of the Mn-1 sample showed very low intensity and the amount of consumed H_2 was 1.8 μmol g^{-1}, which corresponded to a Mn average oxidation state of 2.3.

As expected, the introduction of Mn by sol−gel synthesis induced a remarkable change in the TPR curve shape and in the H_2 consumption, with respect to the impregnation procedure, being responsible for the formation of a mixture of oxidation states.

The different reducibility of the MnO_x species, driven also by the strength of the interaction with the support, is responsible of the observed broadened TPR profile. However, the sol−gel method favors a strong Mn−TiO_2 interaction,

likely enhancing the reduction of the MnO_x species with respect to unsupported Mn_2O_3 and Mn_3O_4 with a consequent shift of the reduction onset to lower T values.[10,27,61] This modulation of Mn reducibility could (positively) affect the NO_x catalytic conversion, thus impacting the SCR activity of the Mn-doped TiO_2 samples.

Another physico-chemical property, which may affect the NH_3-SCR catalytic activity, is surface acidity; Figure 8 shows
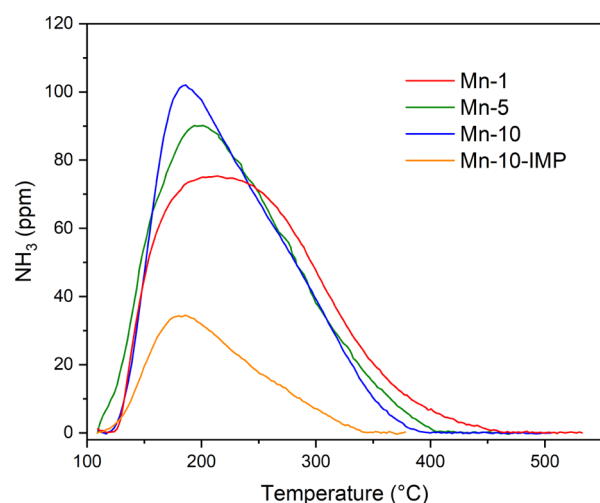
Figure 8. NH_3-TPD curves of Mn-1 (red curve), Mn-5 (green curve), Mn-10 (blue curve), and Mn-10-IMP (orange curve) as measured in the 100−550 °C range.

the sample NH_3-TPD profiles in the 100−550 °C range. With respect to the samples prepared by the reverse micelles sol−gel method, the Mn-10-IMP sample showed a smaller amount of desorbed NH_3 (d_{NH_3}) per g of the catalyst (i.e., 75 μmol g^{-1}), in agreement with its smaller SSA value, and a sharper TPD curve in the 125−350 °C range, indicating the occurrence of fewer and weaker acidic sites. The Mn-1 sample (d_{NH_3} = 242 μmol g^{-1}) showed a different shape in a broader T range (125−450 °C), indicating the presence of abundant and heterogeneous acidic sites.[20] The Mn-5 (d_{NH_3} = 244 μmol g^{-1}) and Mn-10 (d_{NH_3} = 244 μmol g^{-1}) samples showed very similar features not only in terms of the amount of acidic sites, but also in terms of the broad TPD curve profile extending in a wide T range, although Mn-5 showed an onset at slightly lower T. As a whole, the Mn-1, Mn-5, and Mn-10 TPD profiles indicated the occurrence of different types of NH_3 adsorbed species with different thermal stabilities at the catalyst surface.[62] Concerning the nature of those acidic sites, that is, Brønsted or Lewis sites, NH_4^+ ions decompose at a lower T with respect to NH_3-Lewis acid site adducts; in agreement with the literature, the desorption at low T (below 200 °C) may be assigned to NH_3 molecules obtained by the decomposition of NH_4^+ ions bound to Brønsted acid sites and the desorption at high T is associated with NH_3 molecules coordinated to Lewis acid sites. The strength of such Lewis acid sites is weak to medium by considering the desorption T range.[63] Brønsted acid sites are also important for the SCR catalytic activity, and they seem to be more abundant with the Mn-5 sample, showing a desorption onset at a slightly lower T and a component at ca. 170 °C.

2.3. Catalytic Activity—NH$_3$-SCR. The results of the catalytic activity, in terms of NO_x conversion and N_2 selectivity, of all the studied catalysts operating under identical experimental conditions are illustrated in Figure 9a,b. All the
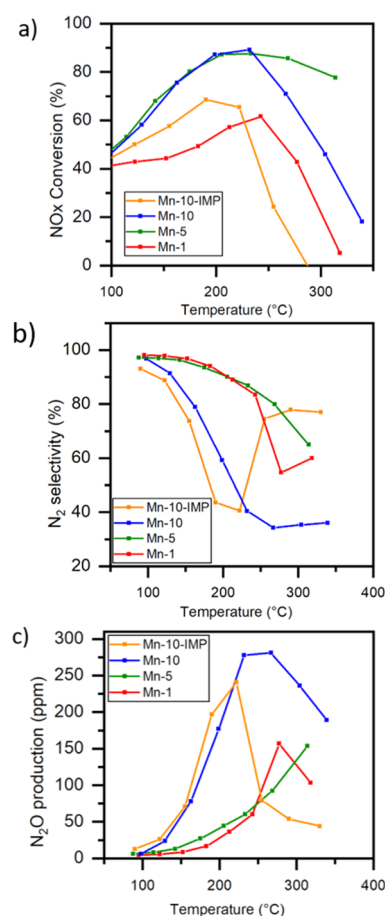
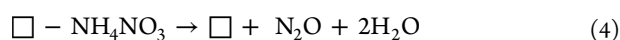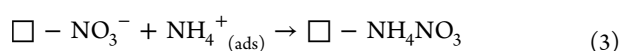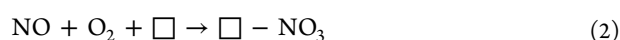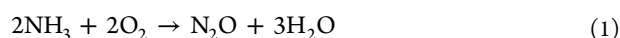**Figure 9.** NO_x conversion (a), N_2 selectivity (b), and N_2O production (c) over the sol gel synthesized and impregnated samples.

conversion curves presented a similar trend as a function of T, with a maximum of conversion followed by a more or less pronounced decline, depicting a "bell" or Gaussian shape rather than a sigmoidal one. This behavior is clearly attributed to the competition of the standard SCR reaction with at least two side reactions, namely, the catalytic oxidation of NH_3 to give either N_2 or N_2O.[64] In fact, beyond the maximum T, the NH_3 oxidation becomes kinetically prevalent, so that the reacting NH_3 is consumed in side reactions, with a consequent decrease in NO_x conversion.

The Mn-5 catalyst showed the best SCR activity, exhibiting both the highest NO_x conversion and the lowest amount of N_2O produced in the 200−250 °C range; the conversion was almost 90%; and the N_2O concentration was ca. 50 ppm. The Mn-10 sample had the same NO_x conversion as Mn-5; however, the selectivity was much lower (more than five times with respect to the Mn-5 catalyst at the maximum conversion) and high N_2O production was observed, while a lower Mn loading (Mn-1) resulted in lower conversion. With the Mn-10 sample, a rapid increase in the N_2O produced was observed suggesting the prominence of the (parasitic) oxidation of NH_3 that, being oxidized, did not participate in the SCR reaction and this is likely promoted by the high content of the reducible

Mn species present in the Mn-10 catalyst, meaning an increased oxidative behavior. It has been widely demonstrated that the high activity of the Mn-based SCR catalysts is the result of the high NO oxidation and its subsequent adsorption in the form of $NO_{2(ads)}$ over the manganese active sites. Activated ammonia also adsorbs on the same acid sites, and it recombines with nitrites consequently decomposing into N_2 and H_2O.[65] However, the rate of formation of such intermediates (NH_4NO_2 or NH_2NO) depends on the NH_3-SCR reaction rate, that is, favored at low temperatures, in comparison with the nonselective NH_3 oxidation rate, which prevails at high temperatures. N_2O is produced by either overoxidation of NH_3 [reaction 1] at higher T (>250 °C) or formation and decomposition of ammonium nitrate and/or nitrite intermediates at low R [reactions 2 and 3],[17,18,52,66] as shown in the following set of reactions

$$2NH_3 + 2O_2 \rightarrow N_2O + 3H_2O \tag{1}$$

$$NO + O_2 + \square \rightarrow \square - NO_3 \tag{2}$$

$$\square - NO_3^- + NH_4^+{}_{(ads)} \rightarrow \square - NH_4NO_3 \tag{3}$$

$$\square - NH_4NO_3 \rightarrow \square + N_2O + 2H_2O \tag{4}$$

where eq 1 represents the ammonia oxidation, eq 2 represents the nitrate formation, eq 3 represents the ammonium nitrate formation, eq 4 represents the ammonium nitrate decomposition, and $\square$ depicts an active site.

The N_2 selectivity and N_2O production (Figure 9b,c) was highly dependent on the synthesis method and the Mn loading likely due to the competition between the abovementioned reactions and the SCR reaction. One of the widely accepted theories for the TiO_2-based SCR reactions is a bifunctional mechanism whereby NH_3 is activated over the acid sites predominantly located on the TiO_2 support with participation of the −OH terminations of the metal sites and the subsequent reaction with the nitrates.[65,67] An increase of the metal loading shifts the NH_3−NO_x activation predominantly over Mn, and above a certain amount, the mechanism changes and the ammonium nitrate formation and decomposition [reactions 3 and 4] become the primary SCR pathway, favoring the N_2O production. This hypothesis can explain the drastic change in the N_2 selectivity for the sol−gel catalysts with 5 and 10 wt % Mn loading (Mn-5 and Mn-10, respectively), which still showed similar overall NO_x conversion. In fact, the similar amount and nature of the acid sites, as demonstrated by NH_3-TPD reported in Figure 8, justified the very close behavior concerning NO_x conversion, correlated to NH_3 adsorption, while the lower amount and better dispersion of manganese in the Mn-5 catalyst hindered the mechanism of N_2O production previously described and improved the N_2 selectivity. Finally, above 250 °C, the N_2O production and N_2 selectivity decreased because the NH_3 overoxidation produced NO instead of N_2O.

The impregnated sample had much lower NO_x conversion and selectivity (i.e., high N_2O produced per NO converted) that could be attributed to the surface occlusion of the TiO_2 acid sites that typically adsorbs NH_3 and activates it for the further SCR reaction, in agreement with the overall NH_3 desorbed amount determined as by NH_3-TPD (*vide supra*). As evidenced in the previous sections, the contact and interaction between Mn and Ti superficial active sites were highly improved due to the one-pot synthesis and the resulting high dispersion of Mn that was not possible to achieve by conventional impregnation. Indeed, the XRD analysis (Figure 1), the Raman spectroscopy (Figure 3) and the DR UV−vis spectroscopy (Figure 4) demonstrated the high Mn dispersion and that after calcination, the MnO_2 and Mn_2O_3 phases remained amorphous in the sol−gel samples with respect to the impregnated sample, where crystalline pyrolusite was detected. The remarkable low-temperature NO_x SCR activity can be likely attributed to such increased dispersion and to the enhanced contact between the multiple TiO_2 and MnO_x active sites, where NO and NH_3 adsorption occurs, therefore interaction and rearrangement toward NH_4NO_2 and NH_2NO intermediates can take place more easily, mainly on the amorphous phases, improving the NO_x conversion at low temperatures.[68−70]

3. CONCLUSIONS

The physico-chemical characterization results showed that the adopted reverse micelle sol−gel synthesis has an impact on the Mn surface and bulk dispersion and on the strength of Mn/TiO_2 interaction. Specifically, with respect to the traditional impregnation method, the reverse micelle method allowed for a fair dispersion of 1, 5, and 10 wt % Mn both in the bulk and at the surface of TiO_2 NPs, with surface MnO_x species resulting mainly amorphous and characterized by a different redox behavior as compared to those obtained by impregnation (i.e., crystalline pyrolusite).

As compared to the literature, the NH_3-SCR catalytic tests showed that the studied catalysts have enhanced deNO$_x$ activity in NH_3-SCR, notwithstanding the low Mn content; both 5 at 10 wt % Mn catalysts were active at low T, the best catalytic activity being obtained at 5 wt % nominal Mn content.

The ensemble of the characterization techniques and the catalytic tests allowed for figuring out in the set of studied catalysts and "optimal" Mn content (i.e., nominal 5 wt %), corresponding to a material characterized by abundant and probably weaker (Brønsted) acidic sites and well-dispersed Mn-species. The same surface species were stabilized as the strong interaction with the support, as obtained by the reverse micelle sol−gel synthesis, which also favored the formation of lower oxidation states of Mn, that is, Mn(II) and Mn(III), in the surface amorphous MnO_x phases.

As a whole, the reported synthesis procedure could be utilized for those types of application (her, NH_3-SCR), requiring the fair dispersion of metal species and their stabilization by the support.

4. EXPERIMENTAL SECTION

4.1. Synthesis Method. All the chemicals were provided by Sigma-Aldrich (Italy).

Mn-doped and undoped TiO_2 NPs were prepared by the reverse micelle microemulsion sol−gel method[71] using polyoxyethylene (20) oleyl ether (Brij O20) as a surfactant and cyclohexane as an oil phase, and titanium(IV)butoxide 97% (Ti-$(BuO)_4$) and manganese(II) nitrate tetrahydrate [$Mn(NO_3)_2 \cdot 4H_2O$, *purum* p.a. ≥97%] as precursors.

In a typical synthesis, a proper amount of Brij-O20 is dispersed in cyclohexane by stirring at 50 °C. Meanwhile, $Mn(NO_3)_2 \cdot 4H_2O$ is dissolved in distilled water and the aqueous solution is added to the oil/surfactant solution and stirred for 45 min, with the formation of a water in-oil (w/o)

microemulsion of surfactant nanoreactors. Afterward, Ti-(BuO)$_4$ is dropwise added to the emulsion.

The mixture is stirred for 2 h at the constant temperature of 50 °C, and finally, the emulsion is broken by the addition of 2-propanol, followed by sonication. The solid phase is then collected by centrifugation and dried at 100 °C for 24 h, followed by calcination in air at 500 °C for 2 h with a temperature ramp of 2.5 °C min^{-1}. Proper precursor amounts were used in order to obtain Mn wt % nominal contents of 0 wt % (TiO$_2$), 1 wt % (Mn-1), 5 wt % (Mn-5), and 10 wt % (Mn-10). Undoped titania was prepared by the same procedure.

For comparison, a sample with a 10 wt % nominal Mn content (Mn-10-IMP) was prepared by the incipient wetness impregnation method by using the same Mn precursor; the support (i.e., the TiO$_2$ sample prepared by the reverse micelle sol−gel method) was impregnated with few drops of the Mn precursor aqueous solution under stirring at 80 °C. The resulting powder was then calcined by following the same procedure adopted for the other sol−gel prepared samples.

4.2. Methods. X-ray powder diffraction (XRPD) patterns were obtained on an X'Pert Phillips diffractometer operating with Cu Kα radiation (1.541874 Å) and equipped with a PIXcel 1D detector (step: 0.026°2θ; time per step: 2 s). Lattice parameters, crystallite size, and quantitative phase analysis were determined by Rietveld analysis, as implemented in MAUD software.[72] The instrumental broadening was characterized by means of the standard NIST 660a (LaB$_6$).

Raman spectra were collected by means of a Renishaw InVia Reflex microRaman spectrometer (Renishaw plc, Wotton-under-Edge, UK) equipped with a cooled charge-coupled device camera. The Raman source was a diode-pumped solid-state laser (λ_{ex} = 514.5 nm), and the sample inspection was performed through a microscope objective (10×) in back-scattering light collection mode. 5 mW laser power, 5 s of exposure time, and four accumulations were employed to collect each spectrum of the pelletized (to facilitate the surface focusing) powders. 0.1 mW laser power was selected for the pelletized (undoped) TiO$_2$ powder only to prevent the scattering signal saturation of the detector. For each sample, five spectra have been recorded on different regions of the surface. Then, each data set was averaged and the resulting averaged Mn-doped TiO$_2$ spectra were normalized to the averaged (undoped) TiO$_2$ spectrum, with respect to the intensity of the 144 cm^{-1} peak.

N$_2$ adsorption/desorption isotherms at −196 °C were acquired on samples previously outgassed at 200 °C for 2 h (Micromeritics Tristar II) to remove water and other atmospheric contaminants. The sample SSA was calculated according to the BET method; the pore total volume was measured at P/P^0 = 0.99; and the pore size distribution was calculated by applying the BJH (Barrett−Joiner−Hallenda) method to isotherm desorption branch.

FESEM micrographs were taken on a ZEISS Supra 40 FESEM instrument (Carl-Zeiss AG, Oberkochen, Germany) equipped with an EDX probe that was used for semi-quantitative determination of the sample chemical composition; typically, on each samples, five spots (ca. 5 μm^3 volume) were analyzed and the average Ti, O, and Mn contents were calculated.

DR UV−vis spectra of the powders were recorded on a UV−vis Varian Cary 5000 spectrophotometer equipped with a DR integration sphere in the 200−1000 nm range.

XPS analyses were performed on a Versa Probe II Scanning XPS Microprobe spectrometer (Physical Electronics GmbH). The measurements were carried out with a monochromatized Al Kα source (X-ray spot 100 μm) at a power of 24.4 W. Wide scans and high-resolution spectra were acquired in fixed analyzer transmission mode with a pass energy of 117.40 and 29.35 eV, respectively. An electron gun was used for charge compensation (1.0 V 20.0 μA). All the BEs were referenced to the C 1s line at 284.8 ± 0.1 eV for adventitious carbon. Data processing was performed by using the MultiPak software (v. 9.8.0.19).

H$_2$-TPR analysis was carried out on a TPD/R/O (temperature-programmed desorption/reduction/oxidation) 1100 ThermoQuest instrument on ca. 50 mg of the sample. In a typical experiment, the powder was kept under constant flow (20 mL min^{-1}) of 5% H$_2$ in the Ar mixture and heated from room temperature to 800 °C with a ramp of 10 °C min^{-1}. The measured H$_2$ uptake was then normalized to the sample weight, in order to allow comparison.

NH$_3$-TPD (temperature-programmed desorption) analysis was carried out in a quartz bed-fixed reactor connected to a NH$_3$ ND-IR (nondispersive infrared) ABB Uras 14 gas analyzer. In each experiment, ca. 200 mg of the sample was pretreated under N$_2$ flow (100 mL min^{-1}) for 60 min at 500 °C (temperature ramp = 10 °C min^{-1}). Then, a mixture of 2000 ppm NH$_3$ in He (400 mL min^{-1}) was fed into the reactor at 100 °C for the adsorption run, which lasted until the NH$_3$ concentration value reached the initial one. The desorption run was performed under N$_2$ flow (400 mL min^{-1}) first at r.t. to remove the loosely physisorbed fraction and subsequently by increasing the temperature up to 500 °C (temperature ramp = 5 °C min^{-1}).

4.3. Catalytic Activity Measurements. SCR of NO$_x$ was carried out by placing 500 mg of catalyst powder in a fixed bed tubular quartz reactor (inner diameter = 10 mm) under a total feed gas flow rate of 300 N mL min^{-1}, which translates to gas hourly space velocity of about 50,000 h^{-1}, as values above 30,000 h^{-1} are typically used industrially. The gas mixture composition was as follows: 500 ppm NO, 500 ppm NH$_3$, 3% O$_2$, and balance N$_2$.

Catalytic tests were performed under isothermal conditions by increasing T from 50 to 350 °C with steps of 32 °C and by waiting to reach stable T and concentrations of the reactive species before each T increase.

The NO$_x$ concentration was analyzed by means of a NO/NO$_2$ UV Limas gas analyzer (ABB SpA) and the N$_2$O and NH$_3$ concentrations by a ND-IR Uras gas analyzer (ABB SpA).

The NO$_x$ and NH$_3$ conversions and the N$_2$ selectivity were calculated from gas concentration according to the following equations

$$NO_x \ (NO + NO_2) \ \text{conversion}[\%]$$
$$= 100 \times \frac{NO_{x \ in} - NO_{x \ out}}{NO_{x \ in}} \tag{5}$$

$$N_2 \ \text{selectivity}[\%] = 100 \times \frac{N_2}{N_2 + N_2O} \tag{6}$$

$$\text{Yield}[\%] = N_2 \ \text{selectivity} \times NO_x \ \text{conversion} \tag{7}$$

■ ASSOCIATED CONTENT

ⓈⒾ Supporting Information

The Supporting Information is available free of charge at https://pubs.acs.org/doi/10.1021/acsomega.1c03153.

Raman spectra after subtraction of the undoped TiO_2 spectrum; N_2 adsorption/desorption isotherms at -196 °C; FE-SEM micrographs; and Ti 2p XP spectra (PDF)

■ AUTHOR INFORMATION

Corresponding Author

Serena Esposito − *Dipartimento di Scienza Applicata e Tecnologia (DISAT) and INSTM Unit of Torino-Politecnico, Politecnico di Torino, 10129 Torino, Italy;* ⓞ orcid.org/ 0000-0001-9159-0541; Email: serena_esposito@polito.it

Authors

Barbara Bonelli − *Dipartimento di Scienza Applicata e Tecnologia (DISAT) and INSTM Unit of Torino-Politecnico, Politecnico di Torino, 10129 Torino, Italy;* ⓞ orcid.org/ 0000-0002-4716-864X

Olimpia Tammaro − *Dipartimento di Scienza Applicata e Tecnologia (DISAT) and INSTM Unit of Torino-Politecnico, Politecnico di Torino, 10129 Torino, Italy*

Ferenc Martinovic − *Dipartimento di Scienza Applicata e Tecnologia (DISAT) and INSTM Unit of Torino-Politecnico, Politecnico di Torino, 10129 Torino, Italy*

Roberto Nasi − *Dipartimento di Scienza Applicata e Tecnologia (DISAT) and INSTM Unit of Torino-Politecnico, Politecnico di Torino, 10129 Torino, Italy*

Gianfranco Dell'Agli − *Dipartimento di Ingegneria Civile e Meccanica, Università degli Studi di Cassino e del Lazio Meridionale, 03043 Cassino, Frosinone, Italy*

Paola Rivolo − *Dipartimento di Scienza Applicata e Tecnologia (DISAT) and INSTM Unit of Torino-Politecnico, Politecnico di Torino, 10129 Torino, Italy;* ⓞ orcid.org/ 0000-0003-0672-5793

Fabrizio Giorgis − *Dipartimento di Scienza Applicata e Tecnologia (DISAT) and INSTM Unit of Torino-Politecnico, Politecnico di Torino, 10129 Torino, Italy*

Nicoletta Ditaranto − *Dipartimento di Chimica, Università degli Studi di Bari Aldo Moro, 70125 Bari, Italy*

Fabio Alessandro Deorsola − *Dipartimento di Scienza Applicata e Tecnologia (DISAT) and INSTM Unit of Torino-Politecnico, Politecnico di Torino, 10129 Torino, Italy*

Complete contact information is available at:
https://pubs.acs.org/10.1021/acsomega.1c03153

Notes

The authors declare no competing financial interest.

■ REFERENCES

(1) Konsolakis, M. Recent Advances on Nitrous Oxide (N_2O) Decomposition over Non-Noble-Metal Oxide Catalysts: Catalytic Performance, Mechanistic Considerations, and Surface Chemistry Aspects. *ACS Catal.* **2015**, *5*, 6397−6421.

(2) Alunga, K. R.; Ye, Y.-Y.; Li, S.-R.; Wang, D.; Liu, Y.-Q. Catalytic Oxidation of Lignin-Acetoderivatives: A Potential New Recovery Route for Value-Added Aromatic Aldehydes from Acetoderivatives. *Catal. Sci. Technol.* **2015**, *5*, 3746−3753.

(3) Rosenberg, H. S.; Curran, L. M.; Slack, A. V.; Ando, J.; Oxley, J. H. Post Combustion Methods for Control of NOx Emissions. *Prog. Energy Combust. Sci.* **1980**, *6*, 287−302.

(4) Busca, G.; Lietti, L.; Ramis, G.; Berti, F. Chemical and Mechanistic Aspects of the Selective Catalytic Reduction of NO(x) by Ammonia over Oxide Catalysts: A Review. *Appl. Catal., B* **1998**, *18*, 1−36.

(5) Gao, F.; Tang, X.; Yi, H.; Zhao, S.; Li, C.; Li, J.; Shi, Y.; Meng, X. A Review on Selective Catalytic Reduction of NO_x by NH_3 over Mn-Based Catalysts at Low Temperatures: Catalysts, Mechanisms, Kinetics and DFT Calculations. *Catalysts* **2017**, *7*, 199.

(6) Janssen, F. J. J. G.; Van Den Kerkhof, F. M. G.; Bosch, H.; Ross, J. R. H. Mechanism of the Reaction of Nitric Oxide, Ammonia, and Oxygen over Vanadia Catalysts. 1. The Role of Oxygen Studied by Way of Isotopic Transients under Dilute Conditions. *J. Phys. Chem.* **1987**, *91*, 5921−5927.

(7) Wood, S. C. Select the Right NOx Control Technology. *Chem. Eng. Prog.* **1994**, *90*, 32.

(8) Dumesic, J. A.; Topsøe, N.-Y.; Topsøe, H.; Chen, Y.; Slabiak, T. Kinetics of Selective Catalytic Reduction of Nitric Oxide by Ammonia over Vanadia/Titania. *J. Catal.* **1996**, *163*, 409−417.

(9) Ramis, G.; Busca, G.; Bregani, F. On the Effect of Dopants and Additives on the State of Surface Vanadyl Centers of Vanadia-Titania Catalysts. *Catal. Lett.* **1993**, *18*, 299−303.

(10) Deorsola, F. A.; Andreoli, S.; Armandi, M.; Bonelli, B.; Pirone, R. Unsupported nanostructured Mn oxides obtained by Solution Combustion Synthesis: Textural and surface properties, and catalytic performance in NO_x SCR at low temperature. *Appl. Catal., A* **2016**, *522*, 120−129.

(11) Fang, D.; Xie, J.; Hu, H.; Yang, H.; He, F.; Fu, Z. Identification of MnOx Species and Mn Valence States in MnO_x/TiO_2 Catalysts for Low Temperature. *Chem. Eng. J.* **2015**, *271*, 23−30.

(12) Li, J.; Chang, H.; Ma, L.; Hao, J.; Yang, R. T. Low-Temperature Selective Catalytic Reduction of NOx with NH3 over Metal Oxide and Zeolite Catalysts-A Review. *Catalysis Today*; Elsevier B.V., 2011; Vol. *175*; pp 147−156.

(13) Wu, Z.; Jiang, B.; Liu, Y. Effect of Transition Metals Addition on the Catalyst of Manganese/Titania for Low-Temperature Selective Catalytic Reduction of Nitric Oxide with Ammonia. *Appl. Catal., B* **2008**, *79*, 347−355.

(14) Xu, G.; Guo, X.; Cheng, X.; Yu, J.; Fang, B. A Review of Mn-Based Catalysts for Low-Temperature NH_3-SCR: NO: X removal and H_2O/SO_2 resistance. *Nanoscale* **2021**, *13*, 7052−7080.

(15) Liu, C.; Shi, J.-W.; Gao, C.; Niu, C. Manganese Oxide-Based Catalysts for Low-Temperature Selective Catalytic Reduction of NO_x with NH_3: A Review. *Applied Catalysis A: General*; Elsevier B.V. July, 2016; Vol. *522*; pp 54−69.

(16) Zhu, M.; Lai, J.-K.; Tumuluri, U.; Wu, Z.; Wachs, I. E. Nature of Active Sites and Surface Intermediates during SCR of NO with NH_3 by Supported V2O5-WO3/TiO2 Catalysts. *J. Am. Chem. Soc.* **2017**, *139*, 15624−15627.

(17) Yang, J.; Ren, S.; zhou, Y.; Su, Z.; Yao, L.; Cao, J.; Jiang, L.; Hu, G.; Kong, M.; Yang, J.; Liu, Q. In Situ IR Comparative Study on N_2O Formation Pathways over Different Valence States Manganese Oxides Catalysts during NH_3−SCR of NO. *Chem. Eng. J.* **2020**, *397*, 125446.

(18) Liu, Z.; Chen, C.; Zhao, J.; Yang, L.; Sun, K.; Zeng, L.; Pan, Y.; Liu, Y.; Liu, C. Study on the NO_2 Production Pathways and the Role of NO_2 in Fast Selective Catalytic Reduction DeNO$_x$ at Low-Temperature over MnO_x/TiO_2 Catalyst. *Chem. Eng. J.* **2020**, *379*, 122288.

(19) Ettireddy, P. R.; Ettireddy, N.; Mamedov, S.; Boolchand, P.; Smirniotis, P. G. Surface Characterization Studies of TiO_2 Supported Manganese Oxide Catalysts for Low Temperature SCR of NO with NH_3. *Appl. Catal., B* **2007**, *76*, 123−134.

(20) Smirniotis, P. G.; Sreekanth, P. M.; Peña, D. A.; Jenkins, R. G. Manganese Oxide Catalysts Supported on TiO_2, Al_2O_3, and SiO_2: A Comparison for Low-Temperature SCR of NO with NH_3. *Ind. Eng. Chem. Res.* **2006**, *45*, 6436−6443.

(21) Sultana, A.; Sasaki, M.; Hamada, H. Influence of Support on the Activity of Mn Supported Catalysts for SCR of NO with Ammonia. *Catal. Today* **2012**, *185*, 284−289.

(22) Putluru, S. S. R.; Schill, L.; Jensen, A. D.; Siret, B.; Tabaries, F.; Fehrmann, R. Mn/TiO2 and Mn-Fe/TiO2 Catalysts Synthesized by Deposition Precipitation-Promising for Selective Catalytic Reduction of NO with NH3 at Low Temperatures. *Appl. Catal., B* **2015**, *165*, 628−635.

(23) Rossetti, I.; Bonelli, B.; Ramis, G.; Bahadori, E.; Nasi, R.; Aronne, A.; Esposito, S. New Insights into the Role of the Synthesis Procedure on the Performance of Co-Based Catalysts for Ethanol Steam Reforming. *Top. Catal.* **2018**, *61*, 1734−1745.

(24) Esposito, S.; Setaro, A.; Maddalena, P.; Aronne, A.; Pernice, P.; Laracca, M. Synthesis of Cobalt Doped Silica Thin Film for Low Temperature Optical Gas Sensor. *J. Sol-Gel Sci. Technol.* **2011**, *60*, 388−394.

(25) Minieri, L.; Esposito, S.; Russo, V.; Bonelli, B.; Di Serio, M.; Silvestri, B.; Vergara, A.; Aronne, A. A Sol−Gel Ruthenium−Niobium−Silicon Mixed-Oxide Bifunctional Catalyst for the Hydrogenation of Levulinic Acid in the Aqueous Phase. *ChemCatChem* **2017**, *9*, 1476−1486.

(26) Bagnasco, G.; Cammarano, C.; Turco, M.; Esposito, S.; Aronne, A.; Pernice, P. TPR/TPO Characterization of Cobalt-Silicon Mixed Oxide Nanocomposites Prepared by Sol-Gel. *Thermochim. Acta* **2008**, *471*, 51−54.

(27) Esposito, S.; Turco, M.; Bagnasco, G.; Cammarano, C.; Pernice, P. New Insight into the Preparation of Copper/Zirconia Catalysts by Sol-Gel Method. *Appl. Catal., A* **2011**, *403*, 128−135.

(28) Prasad, S.; Kumar, V.; Kirubanandam, S.; Barhoum, A. Engineered Nanomaterials: Nanofabrication and Surface Functionalization. *Emerging Applications of Nanoparticles and Architectural Nanostructures: Current Prospects and Future Trends*; Elsevier Inc., 2018; pp 305−340.

(29) Su, C.; Hong, B.-Y.; Tseng, C.-M. Sol−Gel Preparation and Photocatalysis of Titanium Dioxide. *Catal. Today* **2004**, *96*, 119−126.

(30) Dell'Agli, G.; Esposito, S.; Mascolo, G.; Mascolo, M. C.; Pagliuca, C. Films by Slurry Coating of Nanometric YSZ (8 Mol% Y2O3) Powders Synthesized by Low-Temperature Hydrothermal Treatment. *J. Eur. Ceram. Soc.* **2005**, *25*, 2017−2021.

(31) Wu, Z.; Jiang, B.; Liu, Y.; Zhao, W.; Guan, B. Experimental Study on a Low-Temperature SCR Catalyst Based on MnOx/TiO2 Prepared by Sol-Gel Method. *J. Hazard. Mater.* **2007**, *145*, 488−494.

(32) Kim, Y. J.; Kwon, H. J.; Nam, I.-S.; Choung, J. W.; Kil, J. K.; Kim, H.-J.; Cha, M.-S.; Yeo, G. K. High DeNOx Performance of Mn/TiO2 Catalyst by NH3. *Catalysis Today*; Elsevier, 2010; Vol. *151*; pp 244−250.

(33) Esposito, S. "Traditional" Sol-Gel Chemistry as a Powerful Tool for the Preparation of Supported Metal and Metal Oxide Catalysts. *Materials (Basel)* **2019**, *12*, 668.

(34) Hanaor, D. A. H.; Sorrell, C. C. Review of the Anatase to Rutile Phase Transformation. *J. Mater. Sci.* **2011**, *46*, 855−874.

(35) Shannon, R. D. Revised Effective Ionic Radii and Systematic Studies of Interatomic Distances in Halides and Chalcogenides. *Acta Crystallogr. Sect. A* **1976**, *32*, 751−767.

(36) Tompsett, G. A.; Bowmaker, G. A.; Cooney, R. P.; Metson, J. B.; Rodgers, K. A.; Seakins, J. M. The Raman Spectrum of Brookite, TiO2 (Pbca, Z = 8). *J. Raman Spectrosc.* **1995**, *26*, 57−62.

(37) Pérez-Larios, A.; Hernández-Gordillo, A.; Morales-Mendoza, G.; Lartundo-Rojas, L.; Mantilla, Á.; Gómez, R. Enhancing the H2 Evolution from Water-Methanol Solution Using Mn2+-Mn+3-Mn4+ Redox Species of Mn-Doped TiO2 Sol-Gel Photocatalysts. *Catalysis Today*; Elsevier B.V., 2016; Vol. *266*; pp 9−16.

(38) Sultana, A.; Sasaki, M.; Hamada, H. Influence of Support on the Activity of Mn Supported Catalysts for SCR of NO with Ammonia. *Catalysis Today*; Elsevier, 2012; Vol. *185*; pp 284−289.

(39) Xue, M.; Huang, L.; Wang, J.-Q.; Wang, Y.; Gao, L.; Zhu, J.-h.; Zou, Z.-G. The Direct Synthesis of Mesoporous Structured MnO2/TiO2 Nanocomposite: A Novel Visible-Light Active Photocatalyst with Large Pore Size. *Nanotechnology* **2008**, *19*, 185604.

(40) Hsu, Y.-K.; Chen, Y.-C.; Lin, Y.-G.; Chen, L.-C.; Chen, K.-H. Birnessite-Type Manganese Oxides Nanosheets with Hole Acceptor Assisted Photoelectrochemical Activity in Response to Visible Light. *J. Mater. Chem.* **2012**, *22*, 2733−2739.

(41) Ristić, A.; Mazaj, M.; Arčon, I.; Daneu, N.; Zabukovec Logar, N.; Gläser, R.; Tušar, N. N. New Insights into Manganese Local Environment in MnS-1 Nanocrystals. *Cryst. Growth Des.* **2019**, *19*, 3130−3138.

(42) Deng, Q. R.; Xia, X. H.; Guo, M. L.; Gao, Y.; Shao, G. Mn-Doped TiO2 Nanopowders with Remarkable Visible Light Photocatalytic Activity. *Mater. Lett.* **2011**, *65*, 2051−2054.

(43) Shao, G. Red Shift in Manganese- And Iron-Doped TiO2: A Dft+u Analysis. *J. Phys. Chem. C* **2009**, *113*, 6800−6808.

(44) Esposito, S.; Ditaranto, N.; Dell'Agli, G.; Nasi, R.; Rivolo, P.; Bonelli, B. Effective Inclusion of Sizable Amounts of Mo within TiO2 Nanoparticles Can Be Obtained by Reverse Micelle Sol-Gel Synthesis. *ACS Omega* **2021**, *6*, 5379.

(45) Nasi, R.; Esposito, S.; Freyria, F.; Armandi, M.; Gadhi, T.; Hernandez, S.; Rivolo, P.; Ditaranto, N.; Bonelli, B. Application of Reverse Micelle Sol-Gel Synthesis for Bulk Doping and Heteroatoms Surface Enrichment in Mo-Doped TiO2 Nanoparticles. *Materials (Basel)* **2019**, *12*, 937.

(46) Biesinger, M. C.; Payne, B. P.; Grosvenor, A. P.; Lau, L. W. M.; Gerson, A. R.; Smart, R. S. C. Resolving Surface Chemical States in XPS Analysis of First Row Transition Metals, Oxides and Hydroxides: Cr, Mn, Fe, Co and Ni. *Appl. Surf. Sci.* **2011**, *257*, 2717−2730.

(47) Oku, M.; Hirokawa, K.; Ikeda, S. X-Ray Photoelectron Spectroscopy of Manganese-Oxygen Systems. *J. Electron Spectrosc. Relat. Phenom.* **1975**, *7*, 465−473.

(48) Banerjee, D.; Nesbitt, H. W. XPS Study of Dissolution of Birnessite by Humate with Constraints on Reaction Mechanism. *Geochim. Cosmochim. Acta* **2001**, *65*, 1703−1714.

(49) Nesbitt, H. W.; Banerjee, D. Interpretation of XPS Mn(2p) Spectra of Mn Oxyhydroxides and Constraints on the Mechanism of MnO2 Precipitation. *Am. Mineral.* **1998**, *83*, 305−315.

(50) Banerjee, D.; Nesbitt, H. W. Oxidation of Aqueous Cr(III) at Birnessite Surfaces: Constraints on Reaction Mechanism. *Geochim. Cosmochim. Acta* **1999**, *63*, 1671−1687.

(51) Wang, L.; Huang, B.; Su, Y.; Zhou, G.; Wang, K.; Luo, H.; Ye, D. Manganese Oxides Supported on Multi-Walled Carbon Nanotubes for Selective Catalytic Reduction of NO with NH3: Catalytic Activity and Characterization. *Chem. Eng. J.* **2012**, *192*, 232−241.

(52) Tang, X.; Li, J.; Sun, L.; Hao, J. Origination of N2O from NO reduction by NH3 over β-MnO2 and α-Mn2O3. *Appl. Catal., B* **2010**, *99*, 156−162.

(53) Han, Y.-F.; Chen, F.; Zhong, Z.; Ramesh, K.; Chen, L.; Widjaja, E. Controlled Synthesis, Characterization, and Catalytic Properties of Mn2O3 and Mn3O4 Nanoparticles Supported on Mesoporous Silica SBA-15. *J. Phys. Chem. B* **2006**, *110*, 24450−24456.

(54) Xiong, L.-B.; Li, J.-L.; Yang, B.; Yu, Y. Ti3+ in the Surface of Titanium Dioxide: Generation, Properties and Photocatalytic Application. *Journal of Nanomaterials* **2012**, *2012*, 9.

(55) Xaba, B. M.; De Villiers, J. P. R. Sintering Behavior of TiO2-Supported Model Cobalt Fischer-Tropsch Catalysts under H2 Reducing Conditions and Elevated Temperature. *Ind. Eng. Chem. Res.* **2016**, *55*, 9397−9407.

(56) Xu, Q.; Fang, Z.; Chen, Y.; Guo, Y.; Guo, Y.; Wang, L.; Wang, Y.; Zhang, J.; Zhan, W. Titania-Samarium-Manganese Composite Oxide for the Low-Temperature Selective Catalytic Reduction of NO with NH3. *Environ. Sci. Technol.* **2020**, *54*, 2530−2538.

(57) Petrik, I. S.; Krylova, G. V.; Kelyp, O. O.; Lutsenko, L. V.; Smirnova, N. P.; Oleksenko, L. P. XPS and TPR Study of Sol-Gel Derived M/TiO2 Powders (M=Co, Cu, Mn, Ni). *Him. Fiz. ta Tehnol. Poverhni* **2015**, *6*, 179−189.

(58) Xiong, M.; Gao, Z.; Zhao, P.; Wang, G.; Yan, W.; Xing, S.; Wang, P.; Ma, J.; Jiang, Z.; Liu, X.; Ma, J.; Xu, J.; Qin, Y. In Situ Tuning of Electronic Structure of Catalysts Using Controllable Hydrogen Spillover for Enhanced Selectivity. *Nat. Commun.* **2020**, *11*, 1−10.

(59) Esposito, S.; Silvestri, B.; Russo, V.; Bonelli, B.; Manzoli, M.; Deorsola, F. A.; Vergara, A.; Aronne, A.; Di Serio, M. Self-Activating

Catalyst for Glucose Hydrogenation in the Aqueous Phase under Mild Conditions. *ACS Catal.* **2019**, *9*, 3426−3436.

(60) Esposito, S.; Dell'Agli, G.; Marocco, A.; Bonelli, B.; Allia, P.; Tiberto, P.; Barrera, G.; Manzoli, M.; Arletti, R.; Pansini, M. Magnetic Metal-Ceramic Nanocomposites Obtained from Cation-Exchanged Zeolite by Heat Treatment in Reducing Atmosphere. *Microporous Mesoporous Mater.* **2018**, *268*, 131−143.

(61) Esposito, S.; Turco, M.; Bagnasco, G.; Cammarano, C.; Pernice, P.; Aronne, A. Highly Dispersed Sol-Gel Synthesized Cu-ZrO2 Materials as Catalysts for Oxidative Steam Reforming of Methanol. *Appl. Catal., A* **2010**, *372*, 48−57.

(62) Shen, B.; Liu, T.; Zhao, N.; Yang, X.; Deng, L. Iron-Doped Mn-Ce/TiO2 Catalyst for Low Temperature Selective Catalytic Reduction of NO with NH3. *J. Environ. Sci.* **2010**, *22*, 1447−1454.

(63) Zhan, S.; Zhu, D.; Qiu, M.; Yu, H.; Li, Y. Highly Efficient Removal of NO with Ordered Mesoporous Manganese Oxide at Low Temperature. *RSC Adv.* **2015**, *5*, 29353−29361.

(64) Kapteijn, F.; Vanlangeveld, A. D.; Moulijn, J. A.; Andreini, A.; Vuurman, M. A.; Turek, A. M.; Jehng, J. M.; Wachs, I. E. Alumina-Supported Manganese Oxide Catalysts. *J. Catal.* **1994**, *150*, 94−104.

(65) Ettireddy, P. R.; Ettireddy, N.; Boningari, T.; Pardemann, R.; Smirniotis, P. G. Investigation of the selective catalytic reduction of nitric oxide with ammonia over Mn/TiO_2 catalysts through transient isotopic labeling and in situ FT-IR studies. *J. Catal.* **2012**, *292*, 53−63.

(66) Mihai, O.; Widyastuti, C. R.; Kumar, A.; Li, J.; Joshi, S. Y.; Kamasamudram, K.; Currier, N. W.; Yezerets, A.; Olsson, L. The Effect of NO_2/NO_x Feed Ratio on the NH_3-SCR System Over Cu-Zeolites with Varying Copper Loading. *Catal. Lett.* **2014**, *144*, 70−80.

(67) Xie, S.; Li, L.; Jin, L.; Wu, Y.; Liu, H.; Qin, Q.; Wei, X.; Liu, J.; Dong, L.; Li, B. Low Temperature High Activity of M (M = Ce, Fe, Co, Ni) Doped $M-Mn/TiO_2$ Catalysts for NH_3-SCR and in Situ DRIFTS for Investigating the Reaction Mechanism. *Appl. Surf. Sci.* **2020**, *515*, 146014.

(68) Huang, J.; Huang, H.; Liu, L.; Jiang, H. Revisit the Effect of Manganese Oxidation State on Activity in Low-Temperature NO-SCR. *Mol. Catal.* **2018**, *446*, 49−57.

(69) Andreoli, S.; Deorsola, F. A.; Galletti, C.; Pirone, R. Nanostructured MnO catalysts for low-temperature NO SCR. *Chem. Eng. J.* **2015**, *278*, 174−182.

(70) Lou, X.; Liu, P.; Li, J.; Li, Z.; He, K. Effects of Calcination Temperature on Mn Species and Catalytic Activities of Mn/ZSM-5 Catalyst for Selective Catalytic Reduction of NO with Ammonia. *Appl. Surf. Sci.* **2014**, *307*, 382−387.

(71) Eastoe, J.; Hollamby, M. J.; Hudson, L. Recent Advances in Nanoparticle Synthesis with Reversed Micelles. *Adv. Colloid Interface Sci.* **2006**, *128−130*, 5−15.

(72) Lutterotti, L.; Bortolotti, M.; Ischia, G.; Lonardelli, I.; Wenk, H.-R. Rietveld Texture Analysis from Diffraction Images. *Zeitschrift fur Kristallographie, Supplement*; R. Oldenbourg Verlag GmbH, 2007; Vol. *2007*, pp 125−130.